



Atmospheric mercury in a developed region of eastern China: Interannual variation and gas-particle partitioning

Cheng Chen^a, Xiaofei Qin^{b,**}, Hao Li^a, Haiyan Li^a, Chengfeng Liu^a, Mengxin Fu^a, Xiaohao Wang^c, Juntao Huo^c, Yusen Duan^c, Qingyan Fu^c, Kan Huang^a, Congrui Deng^{a,d,e,*}

^a Center for Atmospheric Chemistry Study, Shanghai Key Laboratory of Atmospheric Particle Pollution and Prevention (LAP), Department of Environmental Science and Engineering, Fudan University, Shanghai, 200433, China

^b School of Environmental and Municipal Engineering, Qingdao University of Technology, Qingdao, 266520, China

^c State Ecologic Environmental Scientific Observation and Research Station for Dianshan Lake, Shanghai Environmental Monitoring Center, Shanghai, 200030, China

^d IRDR ICoE on Risk Interconnectivity and Governance on Weather/Climate Extremes Impact and Public Health, Fudan University, Shanghai, 200433, China

^e Institute of Eco-Chongming (IEC), Shanghai, 202162, China

ARTICLE INFO

Keywords:

Atmospheric mercury

Gas-particle partitioning

Aerosol composition

ABSTRACT

Atmospheric mercury plays a crucial role in the biogeochemical cycle of mercury. This study conducted an intensive measurement of atmospheric mercury from 2015 to 2018 at a regional site in eastern China. During this period, the concentration of particle-bound mercury (PBM) decreased by 13%, which was much lower than those of gaseous elemental mercury (GEM, 30%) and reactive gaseous mercury (GOM, 62%). The gradual decrease in the correlation between PBM and CO, K, and Pb indicates that the influence of primary emissions on PBM concentration was weakening. Moreover, the value of the partitioning coefficient (K_p) increased gradually from $0.05 \pm 0.076 \text{ m}^3/\mu\text{g}$ in 2015 to $0.16 \pm 0.37 \text{ m}^3/\mu\text{g}$ in 2018, indicating that GOM was increasingly inclined to adsorb onto particulate matter. Excluding the influence of meteorological conditions and the primary emissions, the change in aerosol composition is designated as the main trigger factor for the increasing gas-particle partitioning of reactive mercury (RM). The increasing ratio of Cl⁻, NO₃⁻, and organics (Org) in the chemical composition of particle matters (PM_{2.5}), as well as the decrease in the proportion of SO₄²⁻, NH₄⁺, and K⁺, are conducive to the adsorption of GOM onto particles, forming PBM, which led to an increase of K_p and a lag of PBM reduction compared to GEM and GOM under the continuous control measures of anthropogenic mercury emissions. The evolution of aerosol compositions in recent years affects the migration and transformation of atmospheric mercury, which in turn can affect the biogeochemical cycle of mercury.

* Corresponding author. Center for Atmospheric Chemistry Study, Shanghai Key Laboratory of Atmospheric Particle Pollution and Prevention (LAP), Department of Environmental Science and Engineering, Fudan University, Shanghai, 200433, China.

** Corresponding author.

E-mail addresses: 17110740018@fudan.edu.cn (X. Qin), congruideng@fudan.edu.cn (C. Deng).

<https://doi.org/10.1016/j.heliyon.2023.e19786>

Received 8 July 2023; Received in revised form 30 August 2023; Accepted 31 August 2023

Available online 21 September 2023

2405-8440/© 2023 The Authors. Published by Elsevier Ltd. This is an open access article under the CC BY-NC-ND license (<http://creativecommons.org/licenses/by-nc-nd/4.0/>).

1. Introduction

Mercury (Hg) is known to cause significant harm to the environment and living organisms due to its persistent, bioaccumulative, and neurotoxic characteristics [1,2]. Atmospheric mercury exists in three forms: gaseous elemental mercury (GEM), reactive gaseous mercury (GOM), and particle-bound mercury (PBM), GOM and PBM are collectively known as reactive mercury (RM). As the dominant form (accounting for 95%) of atmospheric mercury, GEM is relatively stable with a long atmospheric lifetime (~0.5–2 years) due to its relatively high vapor pressure and very low water solubility [3–5]. In contrast, although RM accounts for only about 5% of atmospheric mercury, its characteristics of higher water solubility and chemical reactivity result in a short atmospheric residence time (hours to days) [3,6]. Compared to GEM, RM is easier to remove from the atmosphere through dry and wet deposition [7–9], which not only breaks the equilibrium of the three forms of mercury in the atmosphere but also promotes the biogeochemical cycle of mercury. In addition, RM is also removed from the atmosphere by different physical processes (such as a wet and dry deposition) and deposited at different rates [10], therefore accurate knowledge of RM distribution in the gaseous and particle phases is essential to estimate the mercury deposition and geochemical cycling of mercury.

RM can be semi-volatile under specific circumstances, leading to its partitioning between the gaseous and particle phases [11]. Besides the intensity of the emission sources, the level and composition of RM in the atmosphere are also influenced by various atmospheric physicochemical processes, including the oxidation of GEM, the gas-particles partitioning of oxidation products, and their deposition process to the surface. The gas-particle partitioning of RM is a critical process for interpreting the fluctuations of variable atmospheric Hg forms and the geochemical cycle of mercury [12–15]. GOM and PBM can be interconverted through a gas-particle partitioning process, which can be described in terms of partitioning coefficient K_p . Previous research has shown that K_p strongly depends on the temperature in both dry urban and laboratory aerosols, and it is also influenced by the particle compositions [11,16]. The effects of temperature and aerosol chemical compositions on RM gas-particle partitioning have been further validated in subsequent studies [13,17–20]. Amos et al. employed an empirical partitioning model to perform regression analysis on data from five sites in the United States, emphasizing the importance of gas-particle partitioning and applying simulation results to the GEOS-Chem model. Xu et al. investigated the relationship between K_p and aerosol composition through measured data in Ningbo, China, and found that K_p increased with the increase of organic matter, nitrate, and chloride fractions in the aerosol, while it decreased with the increase of sulfate and ammonium salt fraction. Subsequent studies have shown that relative humidity (RH) can affect the RM gas-particle partitioning process by promoting particle growth and increasing the particle adsorption surface area [18,20,21]. A study by Nguyen et al. at the Lulin site in Taiwan demonstrated that when RH is less than 30%, K_p increases with the increase of RH, and when RH is greater than 30%, K_p decreases with the increase of RH [18].

Accurate knowledge of the distribution of RM in the gaseous and particle phases is essential when using chemical transport models to assess the mercury cycle [22]. RM was entirely regarded as a gas phase or at a fixed rate in the early model assessment of the mercury cycle [23–26], which did not match the actual atmospheric environment because of the variable geographical characteristics and environmental conditions [13,17]. To improve the estimation of mercury circulation in the chemical transport model, Cheng et al. established a model of RM gas-particle partitioning and temperature by linear regression analysis of the data and used it to determine the distribution of RM in the gaseous and particle phases. In recent years, China has implemented strict air pollution control measures, resulting in a significant decline in the level of air pollutants, including mercury, while the chemical compositions of particulate matter have also changed [14,27,28]. These changes could inevitably affect the physical and chemical behavior of atmospheric mercury. Therefore, it is important to study the gas-particle partitioning of RM and its recent changes.

In this study, we conducted continuous and high-resolution measurements of GEM, GOM, and PBM, together with the common composition of particle matter from 2015 to 2018 were carried out at a state super atmospheric observatory located in the most developed Yangtze River Delta (YRD) region in China. We investigated the changing trends, seasonal and diurnal characteristics of

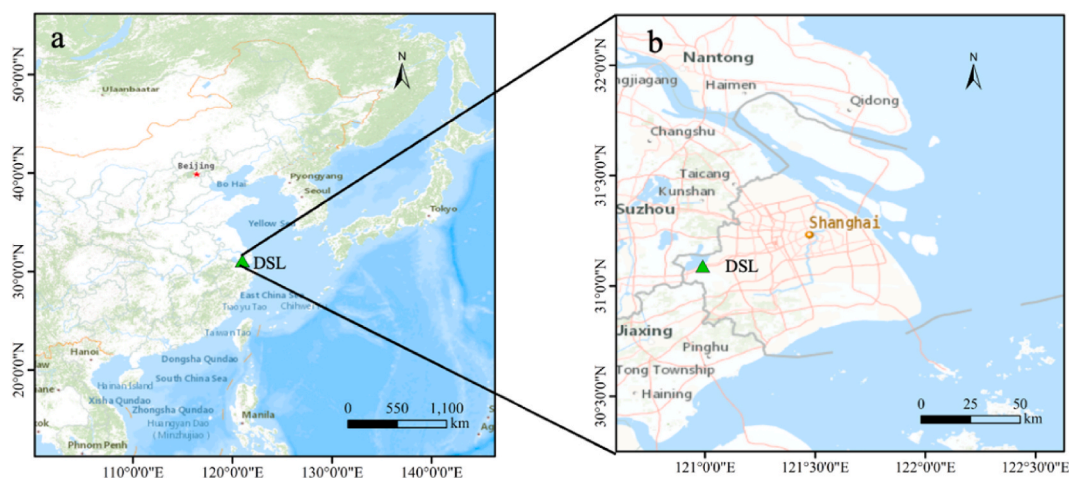


Fig. 1. The location of the Dianshan Lake (DSL) site in Shanghai (b), China (a).

GEM, GOM, and PBM, further explored the gas-particle partitioning of RM and interpreted the increasing trends of K_p , and then clarified the effect of temperature and aerosol chemical composition on the gas-particle partitioning of GOM and PBM.

2. Materials and methods

2.1. Site description

The Atmospheric Super Observatory at Dianshan Lake (DSL) is located in rural Shanghai (31.09°N, 120.98°E) and has a rooftop height of approximately 14 m. All relevant atmospheric components and meteorological parameters were measured at this site, as shown in Fig. 1. Situated at the junction of Shanghai, Jiangsu Province, and Zhejiang Province, the super-station is an ideal site for the observation of air quality over the YRD region and also benefits to understand the regional-scale transport of air pollutants in China. There are no major industrial emission sources within 20 km of the site, such as coal-fired power plants, ferrous metal smelting, cement production, etc [14].

2.2. Measurements of atmospheric mercury

Online concentrations of GEM, GOM, and PBM were acquired from January 2015 to December 2018 via an automated Tekran 2537 B/11301135 system (Tekran Inc., Toronto, Canada) that employs cold vapor atomic fluorescence spectrometry (CVAFS). This system is currently a popular means for atmospheric mercury detection worldwide [29]. At a flow rate of 1 L/min, GEM was collected every 5 min, whereas GOM and PBM were less frequently collected at a flow rate of 10 L/min, with a sampling interval of 2 h. After collection, GOM and PBM underwent thermal decomposition to Hg^0 at temperatures of 500 °C and 800 °C, respectively, before being analyzed by CVAFS. Sampling and measurement adhered to established quality control protocols. According to Tekran technical guidelines, the KCl-coated stripper, Teflon-coated glass inlet, and impact plate underwent weekly replacement, while the quartz filter was changed every month. Calibration of the Tekran 2537 B system was performed routinely every 47 h, utilizing an internal mercury source, and cross-calibrated using an external mercury source every three months. A two-point calibration, involving zero and range calibration, was performed on both gold tubes. To ensure the accuracy of automatic calibration, manual injection with saturated mercury vapor was administered as a cross-verification step.

2.3. Measurements of other air pollutants and meteorological parameters

Thermo Fisher 1405-F, 48i-TLE, 43i, 42i, and 49i instruments were utilized to determine concentrations of $PM_{2.5}$, carbon monoxide (CO), sulfur dioxide (SO_2), nitrogen dioxide (NO_2), and ozone (O_3), while the Monitor of Aerosols and Gases (MARGA) was employed to simultaneously measure water-soluble inorganic ions (SO_4^{2-} , NO_3^- , Cl^-) and cations (K^+ , Mg^{2+} , Ca^{2+} , and NH_4^+) in $PM_{2.5}$. The operational mechanism of the monitor has been elaborated in a prior study [14]. Analysis of organic carbon (OC) and elemental carbon (EC) was conducted utilizing Organic Carbon and Elemental Carbon Aerosol Analyzers (OCEC analyzer, RT-3195, Sunset Laboratory, Beaverton, Oregon, USA). More details were given in Ref. [30].

Hourly meteorological data, including temperature (T), relative humidity (RH), wind speed (WS), and rainfall (P), were recorded synchronously in real-time using an automatic weather station (AWS) located at the monitoring site. All data underwent processing to ensure consistent temporal resolution with the RM samples.

2.4. Reactive mercury gas-particle partitioning model

Partition coefficient (K_p) is used to express the gas-particle partition of RM, which is calculated from GOM, PBM, and $PM_{2.5}$. The calculation formula is as follows (Eq. (1)) [11].

$$K_p = \frac{PBM/PM_{2.5}}{GOM} \quad (1)$$

where the unit of the coefficient K_p is $m^3/\mu g$; PBM is the concentration of particle-bound mercury (pg/m^3); GOM is the concentration of reactive gaseous mercury (pg/m^3); $PM_{2.5}$ is the concentration of fine particles less than or equal to 2.5 μm in diameter (mg/m^3). PBM , GOM , and $PM_{2.5}$ in Eq. (1) are the mean concentration every 2-h.

To understand the effect of temperature on the gas-particles distribution of RM, we introduced the K_p -temperature model [11,13,17]. That is, a linear regression was performed between $\log(1/K_p)$ and $1/T$ shown below (Eq. (2)).

$$\text{Log}(K_p^{-1}) = a + \frac{b}{T} \quad (2)$$

where a and b are regression coefficients, and T is the atmospheric temperature in K. After data processing, we obtained a total of 10,432 pairs of $\log(1/K_p)$ and $1/T$ data. The temperature box averaging method was then used to better describe the relationship between K_p and T [13,19,20]. In this study, the temperature range was -8 °C– 40 °C and the temperature interval was set to 1 °C. For the statistical significance of the data, there are at least 10 data pairs in each temperature interval, otherwise, the temperature interval is discarded.

3. Results and discussion

3.1. General characteristics of atmospheric mercury

3.1.1. Variation trend and concentration level of atmospheric mercury

Fig. 2a illustrates the atmospheric mercury concentrations over the four years from 2015 to 2018. The mean concentrations of GEM, GOM, and PBM during the study period were $2.54 \pm 1.31 \text{ ng/m}^3$, $52.3 \pm 84.6 \text{ pg/m}^3$, and $53.4 \pm 60.8 \text{ pg/m}^3$, respectively. As indicated in Table S1, the mean GEM and PBM concentrations in Shanghai are higher than those measured in some remote areas of China (e.g., Lulin, Chongming, and Mt. Waliguan) and urban and remote sites in other countries (e.g., Fukuoka in Japan; Chicago and Reno in the USA; Mt. Pic du Midi in France), while lower than those reported in urban and suburban sites in China, such as Beijing, Guiyang, Xiamen, and Ningbo [19,20,31,32]. Variability in GEM and PBM concentrations among different sites can be attributed to local anthropogenic mercury emission sources, as well as to regional air mass transport [14,33,34]. Moreover, the GOM concentration in Shanghai was found to be 2–9 times higher than other remote and suburban sites in China (e.g., Lulin, Chongming, and Mt. Waliguan) [18,35,36], and around the world (e.g., Fukuoka in Japan; Chicago and Reno in the USA) [37–39]. However, the GOM concentration in Shanghai was only lower than that of individual domestic coastal urban sites (e.g., Xiamen and Ningbo) [19,32]. It has been reported that offshore areas frequently exhibit relatively high levels of reactive mercury in several subsequent studies [40,41]. The high GOM concentrations observed in Shanghai may be due to strong anthropogenic emissions [14], and may also be related to the fact that because of its coastal location, Shanghai has high levels of atmospheric oxidants, especially bromine atoms, which can oxidize large amounts of GEM to GOM [24].

The inter-annual change in concentrations of GEM, GOM, and PBM are presented in Fig. 2b, displaying a distinct downward trend from 2015 to 2018. Specifically, the GEM concentration decreased from $3.07 \pm 1.6 \text{ ng/m}^3$ in 2015 to $2.01 \pm 0.92 \text{ ng/m}^3$ in 2018. The GOM concentration decreased from $64.9 \pm 89.5 \text{ pg/m}^3$ in 2015 to $24.6 \pm 51.2 \text{ pg/m}^3$ in 2018, while the PBM concentration slightly decreased from $57.8 \pm 64.9 \text{ pg/m}^3$ in 2015 to $50.2 \pm 67.2 \text{ pg/m}^3$ in 2018. The mean concentrations of GEM and GOM decreased by approximately 30% and 62%, respectively, whereas the concentration of PBM only experienced a reduction of about 13% (Fig. 2b). This trend may be attributed to the fact that GEM and GOM are mainly influenced by primary emissions, which have experienced a significant reduction in recent years in China [14,28]. Similar declining patterns were observed for gaseous pollutants such as $\text{PM}_{2.5}$ and SO_2 (Fig. S1). These results suggest that the air pollution control measures in China, such as coal combustion reductions and applying the most advanced pollution control technologies to coal-fired power plants, have achieved initial success [27,28,42].

It should be noted that the relatively low reduction ratio of PBM may be due to the influence of the gas-particle partitioning of RM. Indeed, we investigated the annual mean of GOM/PBM ratios of DSL from 2015 to 2018 and found that the ratios decreased significantly from 1.56 ± 1.97 in 2015 to 1.17 ± 2.8 in 2018, indicating an upward trend in the proportion of PBM to RM.

3.1.2. Monthly and seasonal variations

Fig. S2a and Fig. S2b show the monthly and seasonal variations of atmospheric mercury. In this study, the monthly mean concentrations of GEM exhibited relatively small variations, with the mean value ranging from 1.47 (August 2018) to 4.42 ng/m^3 (January

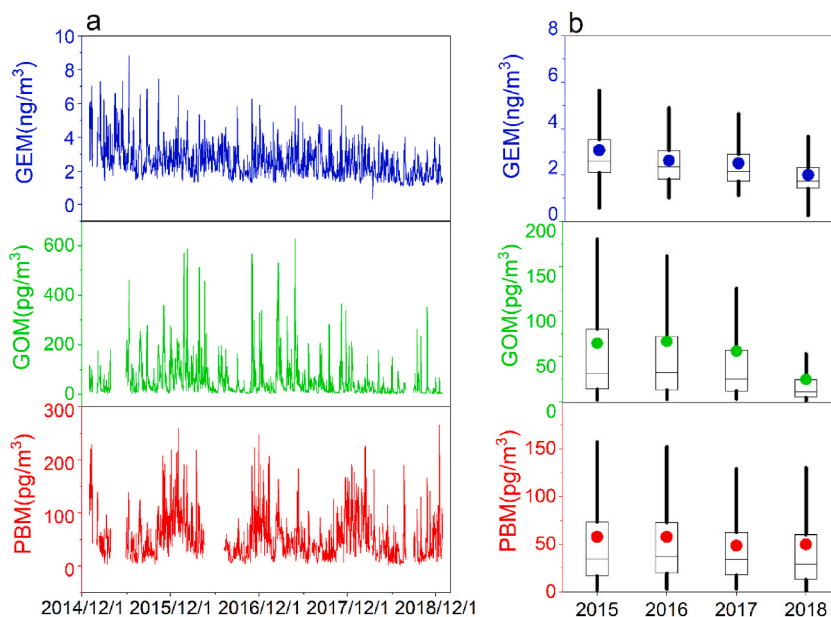


Fig. 2. Hourly (a) and interannual (b) variations of gaseous elemental mercury (GEM), particle-bound mercury (PBM), and reactive gaseous mercury (GOM) concentrations for the entire study period at the Dianshan Lake (DSL).

2015) (Fig. S2a). Throughout the study period, the mean GEM concentrations were higher in spring ($2.74 \pm 1.37 \text{ ng/m}^3$) and winter ($2.72 \pm 1.30 \text{ ng/m}^3$) compared to summer ($2.46 \pm 1.39 \text{ ng/m}^3$) and autumn ($2.28 \pm 1.11 \text{ ng/m}^3$) (Fig. S2b). Similar seasonal patterns were observed in other locations in China, such as Xiamen, Lulin, and Changbai Mountain [8,18,32]. The increased burning of fossil fuels for heating demand is the primary reason for the elevated in atmospheric GEM levels during winter, especially in northern China [43]. However, the concentration gap between the cold and warm seasons in this study was not as pronounced as that observed in the aforementioned locations, possibly due to the less heating demand in cold season as well as the stronger natural emissions from soil, vegetation, and water caused by the increased summer temperatures in the Yangtze River Delta region (Fig. S3)[44]. The uptake of GEM by vegetation may influence the seasonal variation of GEM on a global scale [45].

In this study, the monthly mean concentrations of PBM and GOM exhibited significant fluctuations (Fig. S2a), with the mean values ranging from 20.5 pg/m^3 (August 2016) to 126.2 pg/m^3 (January 2015) for PBM, and from 12.0 pg/m^3 (May 2018) to 126.5 pg/m^3 (February 2017) for GOM. This is similar to many urban locations in China due to the combined impact of emissions and seasonal meteorological conditions [18,32]. As shown in Fig. S4, the planetary boundary layer (PBL) in DSL was highest in August, facilitating the diffusion of air pollutants, which could partly explain the lowest PBM concentration occurred in August. Furthermore, the high temperature in August might cause a shift in the gas-particle balance, inhibiting the adsorption of GOM on particulate matter. Meanwhile, high temperature will promote the formation of GOM, which could explain why the lowest concentration of GOM was not observed in August but in May. In contrast, the concentration of PBM and GOM increased in January and February due to relatively stable atmospheric conditions, the presence of a temperature inversion layer as well as the increased emissions [11,14].

Seasonally, the mean concentrations of PBM ranged from 25.4 pg/m^3 (summer 2016) to 91.2 pg/m^3 (winter 2015), and GOM ranged from 20.3 pg/m^3 (summer 2018) to 106.44 pg/m^3 (winter 2016). The mean PBM concentrations were highest in winter ($81.5 \pm 74.9 \text{ pg/m}^3$), lowest in summer ($32.4 \pm 42.3 \text{ pg/m}^3$), and moderate in spring ($43.5 \pm 47.8 \text{ pg/m}^3$) and autumn ($47.3 \pm 53.8 \text{ pg/m}^3$) throughout the study. Similar seasonal patterns of PBM have been observed in Beijing and Ningbo [19,20]. As can be seen in Fig. S3, the higher concentrations of PBM observed in winter may be attributed to the enhanced fossil fuels combustion, suppressed air dispersion, reduced wet removal processes, and the low temperature which favors the partitioning of RM to the particulate state [11]. As shown in Fig. S2b, the seasonal mean GOM concentrations were comparable in spring ($49.3 \pm 76.7 \text{ pg/m}^3$), summer ($49.0 \pm 80.2 \text{ pg/m}^3$), and autumn ($47.4 \pm 85.5 \text{ pg/m}^3$), but significantly higher in winter ($63.6 \pm 93.7 \text{ pg/m}^3$) throughout the study. Previous studies have rarely reported consistent seasonal patterns of GOM concentrations [33,46]. In this study, the concentration of GOM was highest in summer in 2015, while the highest in winter in 2016. The variation of seasonal distribution might be explained by the

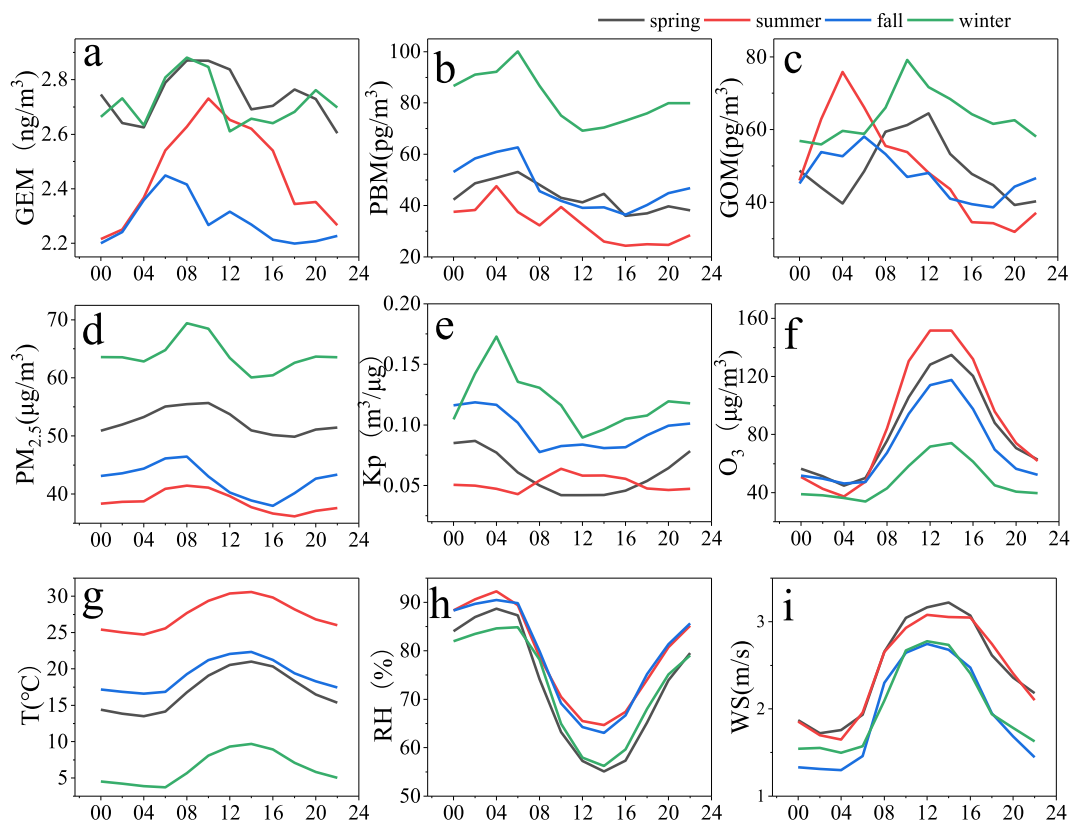


Fig. 3. Daily variation of gaseous elemental mercury (GEM), reactive gaseous mercury (GOM), particle-bound mercury (PBM), particle matters ($\text{PM}_{2.5}$), gas-particle partitioning coefficient (Kp), ozone (O_3), temperature (T), relative humidity (RH), and wind speed (WS) in different seasons during the whole study period.

complexity of the formation process and sources.

3.1.3. Daily variation of atmospheric mercury

GEM, PBM, and GOM mercury concentrations exhibit significant daily variation throughout the study period, but with different patterns (Fig. 3). The elevation of the boundary layer and the enhancement of convection causes a notable decrease in the concentrations of the three kinds of mercury to drop significantly during the daytime, especially at midday. However, due to the differing in sources and formation mechanisms, the three types of mercury exhibit diverse diurnal variation trends.

GEM concentrations peaked around 8 a.m. in all seasons, similar to $PM_{2.5}$ (Fig. 3a and d), possibly because of the sudden increase of anthropogenic activities like coal combustion and traffic emissions [47]. Subsequently, the GEM concentration gradually decreased from 8:00 a.m. (Fig. 3a), probably due to the rising atmospheric boundary layer (PBL) and accelerated oxidation of GEM under an increase of ozone. Additionally, the enhanced wind speed leads to stronger dilution of GEM concentrations and more intense turbulent mixing, especially during midday (Fig. 3i) [48,49].

PBM concentrations peaked at 4–6 a.m. in all seasons and then began to decline until they rose again after 4–6 p.m. (Fig. 3b). The peak in early morning may be due to the lower mixing height at night, and more PBM is captured on the surface following overnight accumulation. The lower concentrations during the midday and early afternoon may be due to the increased convective mixing and dilution [49]. Overall, PBM concentrations are generally higher at night than during the day across all seasons. This phenomenon is consistent with the findings of Schleicher et al. [50], and the reasons for this may be related to the temperature, humidity, solar radiation, and boundary layer dynamics [50,51]. Previous studies have demonstrated that lower nighttime temperatures and higher humidity both contribute to the transfer of reactive mercury from the gas phase to the particle phase [11,18]. Fig. 3g and h show that the lower temperature and higher humidity are observed at night in all seasons, which leads to higher PBM concentration at night than during the day.

Unlike GEM and PBM, daily GOM concentrations show seasonal variation with a peaked value around noon in spring and winter (Fig. 3c), consistent with temperature and ozone concentration levels (Fig. 3f and g), while it appears high concentration in the early morning in summer and autumn. Relatively high concentration of ozone and bromine may promote the oxidation of GEM to GOM, and high temperature favors the transfer of RM to the gas phase [11,15], which might jointly lead to the distinct diurnal variations of GOM.

3.2. Gas-particle partitioning of reactive mercury

As previously mentioned, the decline of PBM (13%) is significantly lower than GOM (62%) from 2015 to 2018. In fact, when compared to other major air pollutants, such as SO_2 (50%), CO (15%), EC (38%), BC (39%), Pb (57%), K (48%) and Cu (47%), PBM exhibited the lowest degree of decline, while GOM showed the highest (Table S2). The adsorption of GOM on particles is a significant source of PBM, and the gas-particle partitioning can impact atmospheric PBM and GOM concentrations. For example, Xu et al. have demonstrated that the contribution of RM gas-particle partitioning to PBM is up to about 40% in winter and at least 28% in other seasons [19]. Therefore, we propose that the large discrepancy in the decline of PBM and GOM concentrations may be attributed to the gas-particle partitioning effect of RM.

Fig. S5 depicts the relationships between PBM and the concentration of CO, K, and Pb during the study period. CO is a commonly used tracer for incomplete combustion, primarily from sources such as motor vehicle exhaust, iron, and steel smelting, and solid waste treatment [52–54]. K is a typical tracer of biomass combustion [14], while Pb mainly arises from gasoline combustion, mining, smelting, and other industrial activities. These pollutants reflect the intensity of primary emissions to some extent. As shown in Fig. S5, there is a positive correlation between PBM and these pollutants, indicating that they are affected by the common primary emissions. However, the correlation coefficients between PBM and those primary emission pollutants gradually decreased from 2015 to 2018, indicating that the impact of primary emissions on PBM is gradually decreasing over time. The ratio of GOM/PBM gradually decreased from 1.56 ± 1.97 in 2015 to 1.17 ± 2.8 in 2018 (Fig. 4a). According to the emission inventory, GOM and PBM accounted for about

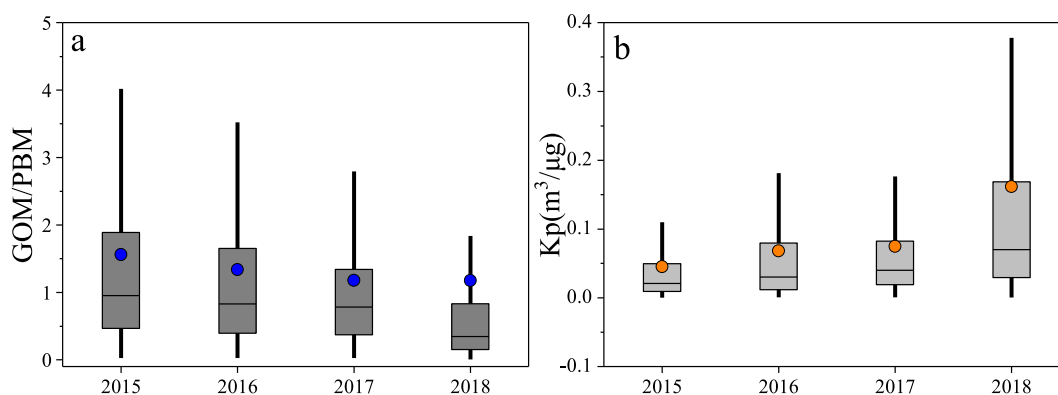


Fig. 4. Interannual variation of reactive gaseous mercury (GOM)/particle-bound mercury (PBM) (a) and gas-particle partitioning coefficient (K_p) (b) during the study period.

46% and 3% of total anthropogenic mercury emissions in China, respectively [34,42,55], and GOM is much higher than PBM. However, in 2018, the PBM concentration is more than two times higher than the GOM concentration, indicating that the gas-particle partitioning of RM might play a crucial role in the formation of PBM.

The Kp value is commonly used to describe the gas-particle partitioning effect of RM. Fig. 4b shows a gradual increase in Kp values from 2015 to 2018, indicating a year-on-year enhancement of the gas-particle partitioning effect. The mean Kp value at the DSL site was $0.16 \pm 0.37 \text{ m}^3/\mu\text{g}$ in 2018, slightly lower than that of other sites in China, such as Lulin ($0.18 \pm 0.40 \text{ m}^3/\mu\text{g}$), Ningbo ($0.24 \pm 0.43 \text{ m}^3/\mu\text{g}$), and Beijing ($0.20 \pm 0.25 \text{ m}^3/\mu\text{g}$), as well as at 10 sites in North America ($0.20\text{--}0.36 \text{ m}^3/\mu\text{g}$) [13,18–20]. In this study, significant seasonal differences and daily variations in Kp values were observed (Fig. 3e). Throughout the study period, Kp values were found to be highest in winter ($0.12 \pm 0.34 \text{ m}^3/\mu\text{g}$), followed by fall ($0.095 \pm 0.13 \text{ m}^3/\mu\text{g}$) and spring ($0.060 \pm 0.090 \text{ m}^3/\mu\text{g}$), while summer exhibited the lowest values ($0.052 \pm 0.086 \text{ m}^3/\mu\text{g}$). It can be seen that Kp is negatively related to temperature with the highest and lowest Kp values corresponding to the lowest and highest seasonal temperatures (Fig. 3e and g).

Moreover, Kp exhibits significant daily variation, with peaking around 4:00 a.m. followed by a declining until reaching the lowest value around noon. The diurnal variation of Kp is exactly opposite to the daily variation of temperature, which further emphasizes the critical role of temperature in driving both seasonal and daily variation of Kp [11]. From a seasonal comparison perspective, higher seasonal temperatures correspond to lower Kp in summer and winter, while the opposite variation occurs in spring and autumn (Fig. 3e and g). This indicates that, in addition to temperature, Kp values are also affected by other factors, such as the aerosol chemical composition and relative humidity, etc [16,18].

3.3. Effect of temperature on the reactive mercury gas-particle partitioning

As shown in Fig. 5a, the equation by linear regression analysis of $\log(1/Kp)$ on $1/T$ is obtained: $\log(1/Kp) = (-2023.2 \pm 150.8) (1/T) + (8.4 \pm 0.5)$. Kp showed a significant negative correlation with T, which indicates that the lower ambient temperature is more favorable for RM partitioning to the particle phase. This negative correlation is consistent with previous studies, but the correlation coefficient in this study ($R^2 = 0.81$) is obvious high (Table 1). The slope of the regression equation in this study is $-2023.2 \mu\text{g K/m}^3$, whose absolute value is smaller than that in Lulin [18] and other stations abroad [13,17,56], but approximately twice that in Beijing [20] and Ningbo (Table 1) [19]. This indicates that the effect of T on gas-particle partitioning is more significant in this study compared to the Chinese urban sites of Beijing and Ningbo.

As illustrated in Fig. 5b, the correlation between Kp and T is found to be the strongest in winter ($R^2 = 0.89$, $p < 0.001$), followed by autumn ($R^2 = 0.69$, $p < 0.001$), summer ($R^2 = 0.47$, $p < 0.001$) and spring ($R^2 = 0.08$, $p < 0.001$). The temperature has a more significant impact on the gas-particle partitioning of RM in winter than in other seasons. The absolute value of the regression equation slope in winter (-3568.9 ± 258.8) was approximately double that of summer (-1889.9 ± 447.6) and fall (-1835.1 ± 243.4), and even 10 times that of spring (-329.5 ± 217.3), which indicated that the conversion of RM from the gaseous to the particle phase is stronger in winter than in other seasons. This seasonal pattern is similar to the reported in Ningbo, China [19], but differs from that in Lulin, Taiwan [18], where the highest correlation and slope were observed in summer.

Although the $\log(1/Kp)$ value decreases with the increase of $1/T$ on the whole, there is an observable increase around $1/T = 0.00345 \text{ K}^{-1}$ (Fig. 5a). This phenomenon is also observed at relatively high ($1/T = 0.00325 \text{ K}^{-1}$) and low ($1/T = 0.00365 \text{ K}^{-1}$) temperatures in Fig. 5a. We find that the similar anomalies in Kp and T around $1/T = 0.00345 \text{ K}^{-1}$ was also showed in the regression curves given by Nguyen et al. [18], but no explanation was provided. To elucidate this anomaly, we analyze the seasonal relationship between Kp and T based on total data of four years, as shown in Fig. 5b. An increasing trend in $\log(1/Kp)$ values at around $1/T = 0.00345 \text{ K}^{-1}$ is found in both spring and autumn seasons. Additionally, an upward trend in $\log(1/Kp)$ values is also found around $1/T = 0.00325 \text{ K}^{-1}$ in summer and $1/T = 0.00365 \text{ K}^{-1}$ in winter (Fig. 5b). This appears to be responsible for the abnormal increase of $\log(1/Kp)$ in Fig. 5a.

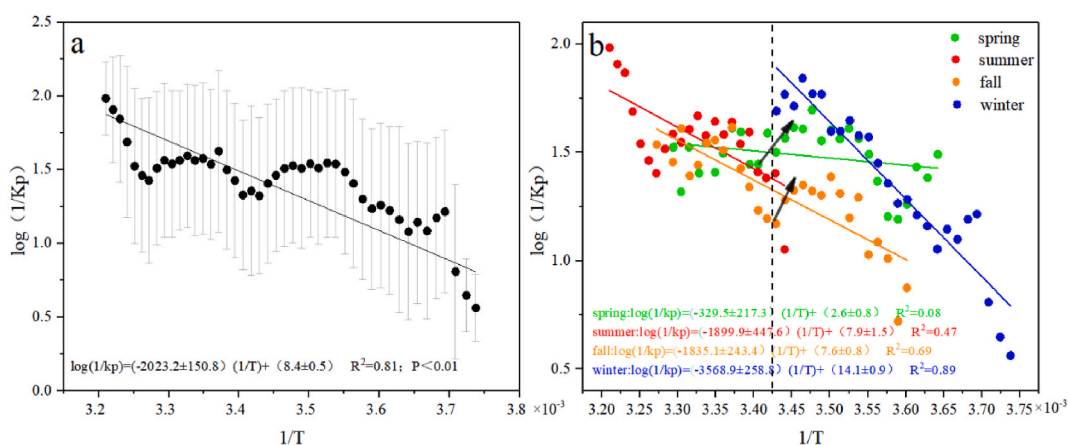


Fig. 5. Relationships between $\log(1/Kp)$ and $1/T$ for (a) the whole study period and (b) the four seasons. (Kp is the gas-particle partitioning coefficient. T is the temperature.)

Table 1

Regression equations for $\log(Kp^{-1}) = a + b/T$ at the Dianshan Lake (DSL) and other sites. (Kp is the gas-particle partitioning coefficient. T is the temperature.)

Site	a	b	R ²	Reference
Dianshan Lake, China	8.4	-2023.2	0.81	This study
Lulin, Taiwan	15.0	-3887.6	0.75	[18]
Beijing, China	5.0	-1082.0	0.24	[20]
Ningbo, China	4.4	-1034.0	0.59	[19]
Yongheung Island, Korea	13.5	-3362.7	0.18	[56]
2 North America sites	12.7	-3485.3	0.55	[13]
5 North America sites	10.0	-2500.0	0.49	[17]
Urban sites in the U.S.	7.0	-1701.0	0.49	[11]

Furthermore, the negative correlations between $\log(1/Kp)$ and $1/T$ in winter and summer are more significant than those in spring and autumn, this can be attributed to the fact that the $1/T$ value is located on the left side of 0.00345 K^{-1} in summer while on the right side in winter, meaning they do not experience a sudden rise in $\log(1/Kp)$ at $1/T = 0.00345\text{ K}^{-1}$. We also observed a common phenomenon of an obvious increase $\log(1/Kp)$ value at around $= 0.00345\text{ K}^{-1}$ occurring in both spring and autumn in all four years (Fig. S6). This seems to indicate that factors other than temperature may significantly affect Kp change when $1/T = 0.00345\text{ K}^{-1}$. Indeed, by fitting the scatter points of each side of $1/T = 0.00345\text{ K}^{-1}$ separately, we found that the correlation between $\log(1/Kp)$ and $1/T$ was significantly better than that of the overall fitting (Fig. S7). In addition, Kp was positively correlated with T during the high temperature in spring in 2017 and summer in 2018 (Fig. S6). These results indicate that, besides temperature, there must be other factors which might significantly affect the gas-particle partitioning of RM in this study.

3.4. Effect of aerosol composition on the reactive mercury gas-particle partitioning

Previous studies have suggested that the particle composition can affect the RM gas-particle partitioning coefficient [16]. It is worth noting that the recent implementation of air pollution control measures in China has not only significantly reduced particulate matter concentrations but also caused substantial changes in its chemical composition [57–60]. Thus, we suppose that the interannual variation of the Kp value may be attributed to changes in particle composition, which could be a key factor influencing the gas-particle partitioning of RM.

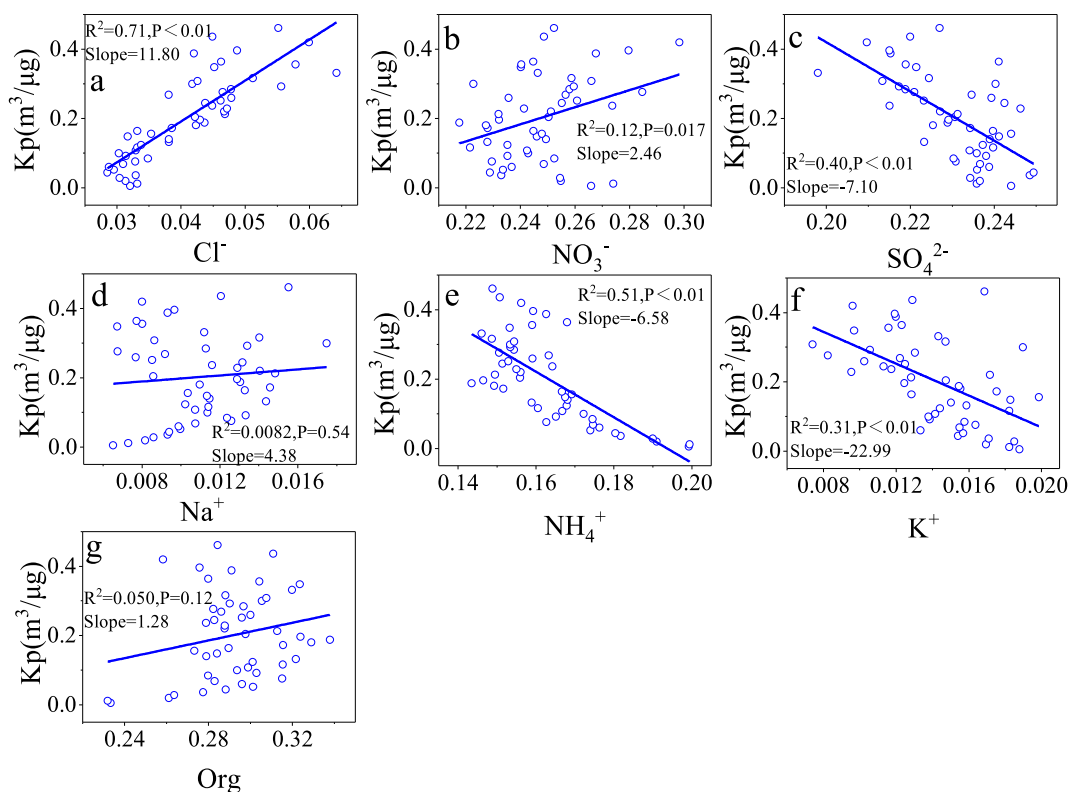


Fig. 6. Relationships between the gas-particle partitioning coefficient (Kp) and the fractions of aerosol chemical components.

As depicted in Fig. S8, the Kp value shows an overall decreasing trend with increasing chemical component concentrations, indicating that the changes in chemical components of the particulate matter does affect the air-particle partition coefficient of RM. From the perspective of individual chemical components, NO_3^- , SO_4^{2-} , NH_4^+ , and Org have a significant negative correlation with Kp, with correlation coefficients of 0.32, 0.55, 0.51, and 0.37, respectively, indicating that these chemical components might affect the RM gas-particle partitioning process. However, it is not appropriate to explain the varying trend of Kp using the absolute concentrations of the chemical components alone, as the concentrations of the chemical components have significantly decreased over the years due to strict air pollution control measures. RM gas-particle partitioning depends on the physical and chemical properties of particulate matters, which are directly related to the composition and mixing state of the co-existence of chemical components. Therefore, considering the proportion of these chemical components in relation to particulate matter would be a better indicator of the variation in Kp. As shown in Fig. 6, Kp generally increased with the increased fraction of Cl^- , NO_3^- , Na^+ , and Org in the aerosol, especially for Cl^- , which shows a significant positive correlation with Kp ($R^2 = 0.71$, $P < 0.01$, Fig. 6a, b, 6d, 6g), and Kp increases rapidly with the increase of Cl^- proportion. Similar positive correlations between Kp and Cl^- , NO_3^- , and Org have been reported in Ningbo [19], but with obvious differences in correlation coefficients, probably due to the fact that the aerosol chemical composition in NR-PM₁ were employed in Ningbo. Some studies have indicated that the proportion of PBM in RM varies considerably in different particle size ranges [61]. Negative correlation are found between Kp and the proportion of SO_4^{2-} , NH_4^+ , and K^+ in the aerosol, with the correlation coefficients (R^2) of 0.40, 0.51, and 0.31, respectively (Fig. 6c, e, 6f).

Based on the field observation, we conclude that sodium nitrate, sodium chloride, and Org in aerosols favor the partition of RM to the particle phase, while ammonium sulfate promotes the partition of RM to the gas phase. Therefore, the annual increase in Kp value over East China is likely attributed to the changes in particulate matter composition in recent years. Indeed, as shown in Fig. 7, the proportions of Cl^- , NO_3^- , and Org in particulate matter, which are positively correlated with Kp, have increased from 48% in 2015 to 59% in 2018. Conversely, the proportions of K^+ , SO_4^{2-} , and NH_4^+ , which are negatively correlated with Kp, have decreased from 50% in 2015 to 40% in 2018. Therefore, the change in the proportion of aerosol components over East China favors the partition of RM to the particle phase, leading to a continuous increase in Kp from 2015 to 2018.

Considering the close relationship between the chemical compositions of aerosols and the gas-particle partitioning of RM, we try to use these compositions to explain the anomalies increase of $\log(1/\text{Kp})$ at $1/T = 0.0035$ (Fig. 5, S5). Fig. 8 depicts the relationship between the proportion of aerosol components and temperature, revealing significant increases or decreases in almost all components at $1/T = 0.0035$. Taking 2015 as an example, we observed that the proportion of Cl^- , Na^+ , and Org in the aerosol suddenly decreased while the proportion of NH_4^+ and SO_4^{2-} sharply increased at $1/T = 0.0035$ (Fig. 8a). This result is consistent with the sudden increase in $\log(1/\text{Kp})$ observed in that year (i.e., Kp suddenly becomes smaller) (Fig. S5a). Based on the relationship between Kp and aerosol chemical composition, these changes in the proportions of chemical components in the aerosol are all conducive to the partitioning of the RM to the gaseous phase. Similar situations can be observed in Fig. 8 in the remaining years (Fig. 8b, c, 8d). These findings also can explain why the correlation between $\log(1/\text{Kp})$ and $1/T$ is weaker in spring and autumn compared to summer and winter in the four

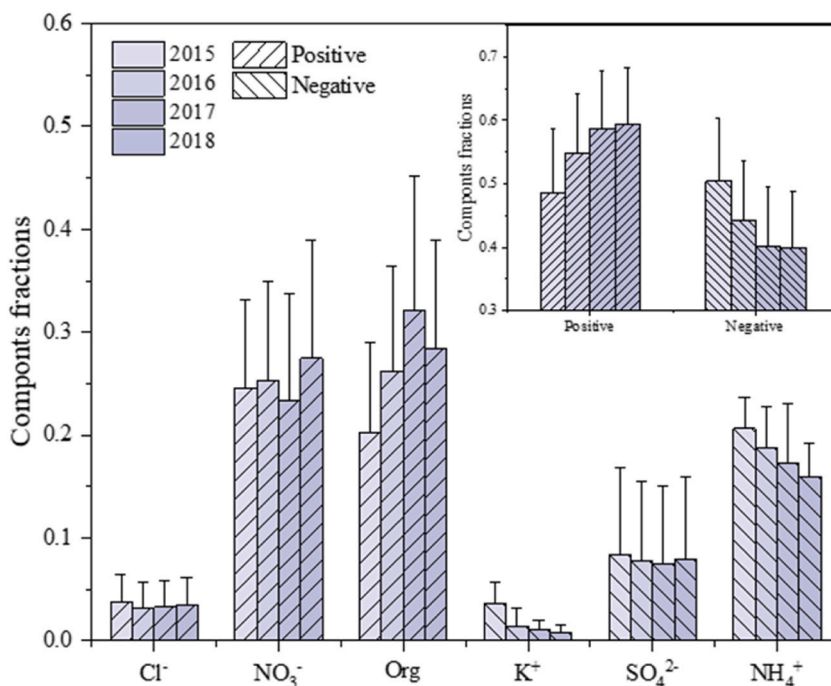


Fig. 7. Annual variation in the fraction of major components in aerosols, where positive represents the sum of chemical components (Cl^- , NO_3^- , Org) with positive correlations and negative represents the sum of chemical components (K^+ , SO_4^{2-} , NH_4^+) with negative correlations.

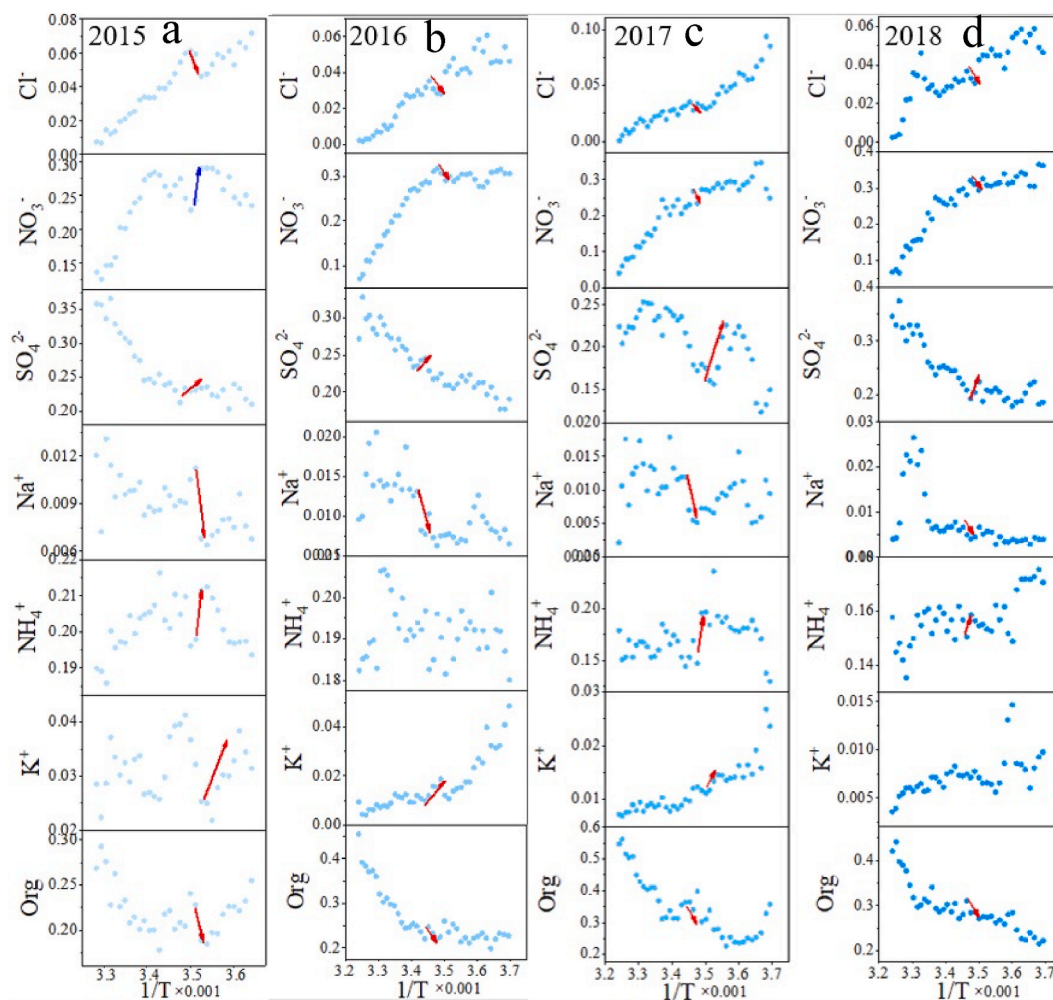


Fig. 8. The relationship between the proportion of aerosol components and $1/\text{temperature}$ (T) in 2015–2018 (a–d).

years study period. Furthermore, the observed positive correlation between K_p and T during the high-temperature period in spring in 2017 and NH_4^+ and T during the high-temperature period in summer in 2018 can also be attributed to the changes in the proportion of aerosol components (Fig. S9).

4. Conclusion

Based on the observations of GEM, GOM, and PBM at the DSL site from 2015 to 2018, the changes in atmospheric mercury concentrations were obtained, and RM gas-particle partitioning as well as their influencing factors were explored. The mean concentrations of GEM, GOM, and PBM decreased from $3.07 \pm 1.6 \text{ ng/m}^3$, $64.9 \pm 89.5 \text{ pg/m}^3$, and $57.8 \pm 64.9 \text{ pg/m}^3$ in 2015 to $2.0 \pm 0.92 \text{ ng/m}^3$, $24.6 \pm 51.2 \text{ pg/m}^3$, and $50.2 \pm 67.2 \text{ pg/m}^3$ in 2018, respectively. The weakening correlation between PBM and CO, K, and Pb indicates that the impact of primary emissions on PBM concentration was decreasing, and gas-particle partitioning became more significant. RM gas-particle partitioning showed seasonal difference, with $\log(1/K_p)$ correlating $1/T$ were better correlated in winter and summer than in spring and autumn, indicating that K_p is also affected by other factors besides temperature. The positive correlation between K_p and Cl^- , NO_3^- , and Org indicates that a high proportion of Cl^- , NO_3^- , and Org is conducive to the adsorption of GOM on particles, while the negative correlation between K_p and SO_4^{2-} , NH_4^+ , and K^+ suggests that a high proportion of SO_4^{2-} , NH_4^+ , and K^+ is not conducive to the conversion of GOM to PBM. Therefore, K_p is also affected by the composition of the aerosol, and the gradual increase of K_p in recent years can be partly attributed to the increase in the proportion of Cl^- , NO_3^- , and Org and the decrease of the proportion of SO_4^{2-} , NH_4^+ , and K^+ in the aerosol. We argue that as the anthropogenic emissions of mercury continue to decrease, the reduction of PBM concentration will lag behind and remain at a relatively high level for a certain period, posing challenges to atmospheric mercury pollution control.

Author contribution statement

Cheng Chen; Congrui Deng; Xiaofei Qin: Conceived and designed the experiments; Wrote the paper. Cheng Chen: Analyzed and interpreted the data. Xiaohao Wang, Juntao Hao, Yusen Duan, Qingyan Fu: Performed the experiments.

Data availability statement

Data will be made available on request.

Additional information

No additional information is available for this paper.

Declaration of competing interest

The authors declare that they have no known competing financial interests or personal relationships that could have appeared to influence the work reported in this paper.

Acknowledgments

This work was financially supported by the National Science Foundation of China (Grants 42275105, 42175119, 21777029).

Appendix A Supplementary data

Supplementary data to this article can be found online at <https://doi.org/10.1016/j.heliyon.2023.e19786>.

References

- [1] E.M. Sunderland, et al., Mercury sources, distribution, and bioavailability in the North Pacific Ocean: insights from data and models, *Global Biogeochem. Cycles* 23 (2) (2009) n/a-n/a.
- [2] L.P. Wright, et al., Impacts and effects indicators of atmospheric deposition of major pollutants to various ecosystems - a review, *Aerosol Air Qual. Res.* 18 (8) (2018) 1953–1992.
- [3] C.T. Driscoll, et al., Mercury as a global pollutant: sources, pathways, and effects, *Environ. Sci. Technol.* 47 (10) (2013) 4967–4983.
- [4] R.P. Mason, G.-R. Sheu, Role of the ocean in the global mercury cycle, *Global Biogeochem. Cycles* 16 (4) (2002) 40–41, 40–14.
- [5] W.H. Schroeder, J. Munthe, Atmospheric mercury - an overview, *Atmos. Environ.* 32 (5) (1998) 809–822.
- [6] S. Lindberg, et al., A Synthesis of Progress and Uncertainties in Attributing the Sources of Mercury in Deposition, *Ambio*, 2007, pp. 19–32.
- [7] G.C. Fang, L. Zhang, C.S. Huang, Measurements of size-fractionated concentration and bulk dry deposition of atmospheric particulate bound mercury, *Atmos. Environ.* 61 (2012) 371–377.
- [8] X.W. Fu, et al., Two years of measurements of atmospheric total gaseous mercury (TGM) at a remote site in Mt. Changbai area, Northeastern China, *Atmos. Chem. Phys.* 12 (9) (2012) 4215–4226.
- [9] N.E. Selin, et al., Chemical cycling and deposition of atmospheric mercury: global constraints from observations, *J. Geophys. Res. Atmos.* 112 (D2) (2007).
- [10] L. Zhang, et al., Estimation of speciated and total mercury dry deposition at monitoring locations in eastern and central North America, *Atmos. Chem. Phys.* 12 (9) (2012) 4327–4340.
- [11] A.P. Rutter, J.J. Schauer, The effect of temperature on the gas-particle partitioning of reactive mercury in atmospheric aerosols, *Atmos. Environ.* 41 (38) (2007) 8647–8657.
- [12] P.A. Ariya, et al., Mercury physicochemical and biogeochemical transformation in the atmosphere and at atmospheric interfaces: a review and future directions, *Chem. Rev.* 115 (10) (2015) 3760–3802.
- [13] I. Cheng, L.M. Zhang, P. Blanchard, Regression modeling of gas-particle partitioning of atmospheric oxidized mercury from temperature data, *J. Geophys. Res. Atmos.* 119 (20) (2014) 11864–11876.
- [14] X.F. Qin, et al., Characteristics of atmospheric mercury in a suburban area of east China: sources, formation mechanisms, and regional transport, *Atmos. Chem. Phys.* 19 (9) (2019) 5923–5940.
- [15] L. Zhang, et al., Atmospheric mercury concentration and chemical speciation at a rural site in Beijing, China: implications of mercury emission sources, *Atmos. Chem. Phys.* 13 (20) (2013) 10505–10516.
- [16] A.P. Rutter, J.J. Schauer, The impact of aerosol composition on the particle to gas partitioning of reactive mercury, *Environ. Sci. Technol.* 41 (11) (2007) 3934–3939.
- [17] H.M. Amos, et al., Gas-particle partitioning of atmospheric Hg(II) and its effect on global mercury deposition, *Atmos. Chem. Phys.* 12 (1) (2012) 591–603.
- [18] L.S.P. Nguyen, et al., Effects of Temperature and Relative Humidity on the Partitioning of Atmospheric Oxidized Mercury at a High-Altitude Mountain Background Site in Taiwan, *Atmospheric Environment*, 2021, p. 261.
- [19] L.L. Xu, et al., Gas-Particle Partitioning of Atmospheric Reactive Mercury and its Contribution to Particle Bound Mercury in a Coastal City of the Yangtze River Delta, China, *Atmospheric Environment*, 2020, p. 239.
- [20] H. Zhang, et al., Concentrations and gas-particle partitioning of atmospheric reactive mercury at an urban site in Beijing, China, *Environ. Pollut.* 249 (2019) 13–23.
- [21] M.M. Lynam, G.J. Keeler, Automated speciated mercury measurements in Michigan, *Environ. Sci. Technol.* 39 (23) (2005) 9253–9262.
- [22] L.M. Zhang, et al., A synthesis of research needs for improving the understanding of atmospheric mercury cycling, *Atmos. Chem. Phys.* 17 (14) (2017) 9133–9144.
- [23] J.O. Bash, et al., Regional air quality model application of the aqueous-phase photo reduction of atmospheric oxidized mercury by dicarboxylic acids, *Atmosphere* 5 (1) (2014) 1–15.
- [24] C.D. Holmes, et al., Global atmospheric model for mercury including oxidation by bromine atoms, *Atmos. Chem. Phys.* 10 (24) (2010) 12037–12057.

- [25] H. Lei, et al., Model analyses of atmospheric mercury: present air quality and effects of transpacific transport on the United States, *Atmos. Chem. Phys.* 13 (21) (2013) 10807–10825.
- [26] N.E. Selin, D.J. Jacob, Seasonal and spatial patterns of mercury wet deposition in the United States: constraints on the contribution from North American anthropogenic sources, *Atmos. Environ.* 42 (21) (2008) 5193–5204.
- [27] J.M. Pacyna, et al., Current and future levels of mercury atmospheric pollution on a global scale, *Atmos. Chem. Phys.* 16 (19) (2016) 12495–12511.
- [28] Y. Tang, et al., Recent decrease trend of atmospheric mercury concentrations in East China: the influence of anthropogenic emissions, *Atmos. Chem. Phys.* 18 (11) (2018) 8279–8291.
- [29] M.S. Landis, G.J. Keeler, Atmospheric mercury deposition to Lake Michigan during the Lake Michigan mass balance study, *Environ. Sci. Technol.* 36 (21) (2002) 4518–4524.
- [30] H. Li, et al., Conjoint Impacts of Continental Outflows and Marine Sources on Brown Carbon in the East China Sea: Abundances, Optical Properties, and Formation Processes, *Atmospheric Environment*, 2022, p. 273.
- [31] X. Fu, et al., Speciated atmospheric mercury and its potential source in Guiyang, China, *Atmos. Environ.* 45 (25) (2011) 4205–4212.
- [32] L. Xu, et al., Characteristics and sources of atmospheric mercury speciation in a coastal city, Xiamen, China, *Chemosphere* 119 (2015) 530–539.
- [33] H. Mao, I. Cheng, L. Zhang, Current understanding of the driving mechanisms for spatiotemporal variations of atmospheric speciated mercury: a review, *Atmos. Chem. Phys.* 16 (20) (2016) 12897–12924.
- [34] L.S.P. Nguyen, et al., Temporal changes in atmospheric mercury concentrations at a background mountain site downwind of the East Asia continent in 2006–2016, *Sci. Total Environ.* 686 (2019) 1049–1056.
- [35] X.W. Fu, et al., Temporal trend and sources of speciated atmospheric mercury at Waliguan GAW station, Northwestern China, *Atmos. Chem. Phys.* 12 (4) (2012) 1951–1964.
- [36] L. Zhang, et al., A synthesis of research needs for improving the understanding of atmospheric mercury cycling, *Atmos. Chem. Phys.* 17 (14) (2017) 9133–9144.
- [37] L.E. Gratz, et al., Atmospheric transport of speciated mercury across southern Lake Michigan: influence from emission sources in the Chicago/Gary urban area, *Sci. Total Environ.* 448 (2013) 84–95.
- [38] S.N. Lyman, M.S. Gustin, Determinants of atmospheric mercury concentrations in Reno, Nevada, USA, *Sci. Total Environ.* 408 (2) (2009) 431–438.
- [39] K. Marumoto, M. Hayashi, A. Takami, Atmospheric mercury concentrations at two sites in the Kyushu Islands, Japan, and evidence of long-range transport from East Asia, *Atmos. Environ.* 117 (2015) 147–155.
- [40] V. Shah, et al., Origin of oxidized mercury in the summertime free troposphere over the southeastern US, *Atmos. Chem. Phys.* 16 (3) (2016) 1511–1530.
- [41] C. Wang, et al., Speciated atmospheric mercury in the marine boundary layer of the Bohai Sea and Yellow Sea, *Atmos. Environ.* 131 (2016) 360–370.
- [42] L. Zhang, et al., Updated emission inventories for speciated atmospheric mercury from anthropogenic sources in China, *Environ. Sci. Technol.* 49 (5) (2015) 3185–3194.
- [43] X. Fu, et al., Observations of atmospheric mercury in China: a critical review, *Atmos. Chem. Phys.* 15 (16) (2015) 9455–9476.
- [44] M. Liu, et al., Mercury export from mainland China to adjacent seas and its influence on the marine mercury balance, *Environ. Sci. Technol.* 50 (12) (2016) 6224–6232.
- [45] M. Jiskra, et al., A vegetation control on seasonal variations in global atmospheric mercury concentrations, *Nat. Geosci.* 11 (4) (2018) 244–250.
- [46] P.A. Ariya, et al., Mercury physicochemical and biogeochemical transformation in the atmosphere and at atmospheric interfaces: a review and future directions, *Chem. Rev.* 115 (10) (2015) 3760–3802.
- [47] D.L. Nguyen, et al., Ground and shipboard measurements of atmospheric gaseous elemental mercury over the Yellow Sea region during 2007–2008, *Atmos. Environ.* 45 (1) (2011) 253–260.
- [48] J. Song, *Observational Studies and Numerical Simulations of Land and Sea Breezes Circulations over East Areas of Ningbo*, Nanjing University of Information Science and Technology, Nanjing, 2008.
- [49] J. Stamenkovic, S. Lyman, M.S. Gustin, Seasonal and diel variation of atmospheric mercury concentrations in the Reno (Nevada, USA) airshed, *Atmos. Environ.* 41 (31) (2007) 6662–6672.
- [50] N. Schleicher, et al., Atmospheric particulate mercury in the megacity Beijing: Spatio-temporal variations and source apportionment, *Atmos. Environ.* 109 (2015) 251–261.
- [51] Y.W. Hong, et al., Pattern of atmospheric mercury speciation during episodes of elevated PM_{2.5} levels in a coastal city in the Yangtze River Delta, China, *Environ. Pollut.* 218 (2016) 259–268.
- [52] S.C. Lai, et al., Characterization and source regions of 51 high-CO events observed during civil aircraft for the regular investigation of the atmosphere based on an instrument container (CARIBIC) flights between south China and the Philippines, 2005–2008, *J. Geophys. Res. Atmos.* (2011) 116.
- [53] S.C. Lai, et al., Pollution events observed during CARIBIC flights in the upper troposphere between South China and the Philippines, *Atmos. Chem. Phys.* 10 (4) (2010) 1649–1660.
- [54] D.D. Parrish, et al., Comparison of air pollutant emissions among mega-cities, *Atmos. Environ.* 43 (40) (2009) 6435–6441.
- [55] Q. Wu, et al., Temporal trend and spatial distribution of speciated atmospheric mercury emissions in China during 1978–2014, *Environ. Sci. Technol.* 50 (24) (2016) 13428–13435.
- [56] G.S. Lee, et al., Atmospheric speciated mercury concentrations on an island between China and Korea: sources and transport pathways, *Atmos. Chem. Phys.* 16 (6) (2016) 4119–4133.
- [57] S.Y. Cai, et al., The impact of the "air pollution prevention and control action plan" on PM_{2.5} concentrations in jing-jin-ji region during 2012–2020, *Sci. Total Environ.* 580 (2017) 197–209.
- [58] Z. Ding, et al., Summertime atmospheric dicarboxylic acids and related SOA in the background region of Yangtze River Delta, China: implications for heterogeneous reaction of oxalic acid with sea salts, *Sci. Total Environ.* 757 (2021), 143741.
- [59] Z. Qi, et al., Revealing contributions to sulfur dioxide emissions in China: from the dimensions of final demand, driving effect and supply chain, *Resour. Conserv. Recycl.* (2020) 160.
- [60] B. Zheng, et al., Trends in China's anthropogenic emissions since 2010 as the consequence of clean air actions, *Atmos. Chem. Phys.* 18 (19) (2018) 14095–14111.
- [61] D. Han, et al., Particulate mercury in ambient air in Shanghai, China: size-specific distribution, gas–particle partitioning, and association with carbonaceous composition, *Environ. Pollut.* 238 (2018) 543–553.